Gas Transport Characteristics of Supramolecular Networks of Metal-Coordinated Highly Branched Poly(ethylene oxide)

Taliehsadat Alebrahim[1], Alisa Chakraborty[1], Leiqing Hu[1], Shalin Patil[2], Shiwang Cheng[2], Durga Acharya[3], Cara M. Doherty[3], Anita J. Hill[3], Timothy R. Cook,[4] and Haiqing Lin*[1]

[1]Department of Chemical and Biological Engineering, University at Buffalo, The State University of New York, Buffalo, NY 14260, USA

[2]Department of Chemical Engineering and Materials Science, Michigan State University, East Lansing, MI 48864, USA

[3]Commonwealth Scientific and Industrial Research Organization (CSIRO) Manufacturing, Private Bag 10, Clayton, Victoria 3169, AU

[4]Department of Chemistry, University at Buffalo, The State University of New York, Buffalo, NY 14260, USA

* Corresponding author: Email: haiqingl@buffalo.edu

Prepared for submission to *Journal of Membrane Science*

ABSTRACT:

Model systems are developed and investigated to better understand the effect of polyether-metal ion interactions on gas separation characteristics. These systems help answer current questions raised by the substantial body of research on metal-organic frameworks (MOFs) dispersed in polyethers to improve gas separation performance, where favorable interactions between the metal centers and polyethers are preferred to improve interfacial compatibility. Specifically, we investigate CO_2/gas transport properties of supramolecular networks comprising cross-linked poly(ethylene oxide) (XLPEO) and dissociable salts, including $LiClO_4$, $Ni(BF_4)_2$, and $Cu(BF_4)_2$. Increasing the salt content increases the glass transition temperature (T_g) and generally decreases gas diffusivity and permeability, which can be successfully described using a T_g-integrated free volume model with an expression similar to the Vogel-Tammann-Fulcher (VTF) equation. Surprisingly, low loadings of $LiClO_4$ and $Cu(BF_4)_2$ (2 mass% or less) can increase gas permeability by 30% - 70% without affecting the CO_2/gas selectivity. This increase correlates with polyether-metal ion dynamics as measured by dielectric spectroscopy. Understanding how interaction-mediated dynamics affect gas transport will be instrumental to designing MOF-based mixed matrix materials for gas separations.

Keywords: Matrix matrix membranes; poly(ethylene oxide); CO_2 separation; metal-organic frameworks; polymer electrolytes

1. Introduction

Polyethers have been widely explored as membrane materials for CO_2/gas separation due to their high affinity towards CO_2 with quadrupole moment [1-5]. For example, poly(ethylene oxide) (PEO)-based polymers contain polar ether oxygens interacting favorably with CO_2, thus exhibiting high CO_2 solubility and CO_2/gas solubility selectivity [2, 4, 6]. Additionally, despite the polar nature, the polyether chains have great flexibility, leading to high CO_2 diffusivity and thus permeability. For example, a cross-linked, highly branched PEO (XLPEO) prepared from 9 mass% poly(ethylene glycol) diacrylate (PEGDA, n = 14) and 91 mass% poly(ethylene glycol) methyl ether acrylate (PEGMEA, n = 8) exhibited CO_2 permeability of 520 Barrer (1 Barrer = 10^{-10} cm^3 (STP) cm cm^{-2} s^{-1} $cmHg^{-1}$) and CO_2/N_2 selectivity of 52 at 35 °C, which is on Robeson's upper bound [7].

To further improve separation properties, polyethers can be doped with porous inorganic fillers with desirable pore size and porosity to form mixed matrix materials (MMMs) [8-13]. For example, metal-organic frameworks (MOFs) and metal-organic polyhedra (MOPs) comprising metal ions covalently tied by organic linkers that form a cage-like microporous structure have been widely explored because of their porous structures, large surface area, and great structural diversity [14-17]. Specifically, introducing 20 mass% ZIF-8 nanoparticles (NPs) in PEGDA-*co*-PEGMEA increased CO_2 permeability from 330 to 840 Barrer while retaining the high CO_2/light gas selectivity [18]; incorporating 30 mass% MOP-3 with NP sizes of ≈5 nm in a polymer derived from poly(1,3 dioxolane) acrylate (PDXLA) increased CO_2 permeability from 190 to 580 Barrer [19]. Compared with MMMs with void formation between the fillers and polymers [12, 19, 20], the polyethers can strongly interact with metal ions of the MOFs and MOPs and then achieve excellent interfacial compatibility [8, 21, 22]. For example, incorporation of 70 mass% UiO66 in

poly(ethylene glycol) (PEG) increased Young's Modulus from 133 to 284 MPa by ~114%, indicating a strong interaction between UiO66 and PEG [21].

While the high porosity of the porous fillers is intuitively credited for the increase in gas permeability in the MMMs, an understanding of the effects of the polymer-metal ion interaction on gas transport properties is lacking. Polymer-metal ion interactions have been tailored to design supramolecular polymer networks and are expected to influence morphology and gas transport properties [23]. Moreover, metal ions (such as Cu^{2+}) have been demonstrated to interact with amine-rich polymers to form micropores, leading to superior CO_2/N_2 separation properties [24]. However, it is impossible to decouple the effects of the porosity of the fillers and the polymer-metal ion interactions on the gas transport properties in these MMMs. For this reason, we designed a material system of XLPEO and dissolved salts with metal ions commonly found in the MOFs and MOPs (such as Cu^{2+} and Ni^{2+}). Coincidently, the ethylene oxide units have been demonstrated to dissociate salts and form complexes with different metal ions [25, 26]. For example, lithium salts such as $LiClO_4$ can be dissolved in XLPEO as polymer electrolytes for battery applications [27]; silver salts such as $AgBF_4$ were dissolved in PEO and showed a strong affinity towards olefins and thus high olefin/paraffin separation properties [28-30]. As a comparison, PEG-based materials were also doped with ionic liquids (ILs) with similar anions, such as 1-butyl-3-methylimidazolium tetrafluoroborate [Bmim][BF_4] [31-34], which act as plasticizers, decreasing T_g and increasing gas diffusivity [31].

In this study, three salts ($LiClO_4$, $Ni(BF_4)_2$, and $Cu(BF_4)_2$) were dissolved in an XLPEO (PEGDA-*co*-PEGMEA with a PEGDA and PEGMEA mass ratio of 1:4), and the effects of metal ions on the structure and gas transport properties are thoroughly investigated. $LiClO_4$ was chosen as its effect on the polymer structure and Li-ion conductivity has been widely reported, but not gas

transport characteristics [27]. Therefore, XLPEO/$LiClO_4$ serves as a reference for XLPEO/$Ni(BF_4)_2$ and XLPEO/$Cu(BF_4)_2$, which directly model some MOF-based MMMs studied in the literature. The salts can be fully dissociated in amorphous XLPEO, increasing glass transition temperature (T_g). The effects of the salt content on gas solubility, diffusivity, and permeability of the supramolecular networks are examined. Surprisingly, low loadings of $LiClO_4$ and $Cu(BF_4)_2$ dramatically increase gas permeability, while a further increase in the salt content decreases gas diffusivity and permeability. The effect of the salt content on the gas diffusivity and permeability can be successfully described using a T_g-integrated free volume model without adjustable parameters. Though the salts might not be safe or stable to be used for practical membrane applications, they can provide valuable insights into the interactions of ions and XLPEO and their impact on gas transport characteristics.

2. Experimental

2.1. Materials

PEGDA (n = 13; Mn = 700 g/mol) and PEGMEA (n = 9; Mn = 480 g/mol), and 1-hydroxycyclohexyl phenyl ketone (HCPK) were purchased from Sigma Aldrich Corporation (St. Louis, MO). $LiClO_4$ and $Cu(BF_4)_2{\cdot}xH_2O$ were received from Sigma Aldrich, and $Ni(BF_4)_2{\cdot}6H_2O$ was procured from Thermo Fisher Scientific (Waltham, MA). The salts were kept in a dry box before use. Gas cylinders of H_2, N_2, CH_4, CO_2, and C_2H_6 (99.99%) were obtained from Airgas Inc. (Buffalo, NY).

2.2. Preparation of supramolecular networks

To prepare supramolecular networks, prepolymer solutions were first prepared using PEGDA, PEGMEA, HCPK (0.1 mass% relative to PEGDA and PEGMEA), and the salt in a

111 solvent (i.e., acetonitrile for $LiClO_4$ and water for $Ni(BF_4)_2$ and $Cu(BF_4)_2$). The mass ratio of
112 PEGDA to PEGMEA was set at 1:4. Second, the solution was sandwiched between two quartz
113 plates separated by spacers with a known thickness. Third, the solution was exposed to UV light
114 with a wavelength of 254 nm at 3.0 mW cm^{-2} for 5 mins for PEGDA and PEGMEA to polymerize
115 [7, 27]. Finally, the solid films were kept in a vacuum oven at 40 °C for 48 h before use. The film
116 thickness was measured using a digital micrometer (Mitutoyo Corporation, Kanagawa, JP). The
117 samples are labeled as XLPEO/salt-*x*, where *x* stands for the mass% of the salt in the dried sample.

118 **2.3. Characterization of supramolecular networks**

119 An attenuated total reflection-Fourier transform infrared (ATR-FTIR) spectrometer (Vertex
120 70, Billerica, MA) was used to investigate the degree of reaction conversion of the PEGDA and
121 PEGMEA and the state of the salts in XLPEO. A total of 100 scans were obtained with
122 wavenumbers ranging from 4000 to 400 cm^{-1} at a resolution of 4 cm^{-1}. X-ray fluorescence (XRF)
123 analysis was used to measure the anhydrous salt content in the XLPEO/salt samples using an
124 Epsilon 1–549 (PANalytical B.V., Netherlands) with a 50 kV silver anode tube as the radiation
125 source.

126 An Ultima IV X-ray diffractometer (Rigaku Corporation, Tokyo, JP) with a CuKa radiation
127 (a wavelength of 1.54 Å), operating in air at ≈ 23 °C, was used to examine structure. Thermal
128 transitions were measured using Differential Scanning Calorimetry (DSC, Q2000, TA Instruments,
129 New Castle, DE). Two heating cycles were obtained from -90 to 60 °C at 10 °C/min in N_2
130 atmosphere. The T_g was defined as the inflection point of the step change during the second heating
131 using Universal Analysis 2000 software.

132 The density of the samples was measured using an analytical balance equipped with a
133 density kit. Iso-octane was used as the auxiliary liquid with a density (ρ_L) of 0.692 g/cm^3. The

sample density, ρ_{PE} (g/cm^3), is calculated using Equation (1) [6, 7]:

$$\rho_{PE} = \frac{m_a \rho_L}{m_a - m_L} \quad (1)$$

where m_a and m_L are the mass of the sample in the air and iso-octane, respectively.

Positron annihilation lifetime spectroscopy (PALS) was used to determine the free volume of the XLPEO/$LiClO_4$ and XLPEO/$Cu(BF_4)_2$ samples under vacuum (1.3×10^{-3} Pa) at 22 °C using an EG&G Ortec (Oak Ridge, TN) fast-fast coincidence spectrometer. A minimum of five spectra with 4.5×10^6 were collected for each sample and fitted using LT-v9 software with a source correction from the Mylar encased NaCl (1.61 ns, 2.45%). Error bars are calculated based on the population standard deviation of five experiments.

The dynamics of the XLPEO/$LiClO_4$ and XLPEO/$Cu(BF_4)_2$ were examined using dielectric measurements. Specifically, disk-like membranes with a thickness of 0.2 mm and diameter of 30 mm were sandwiched by two gold electrodes with a diameter of 20 mm. After that, the sandwiched membranes were loaded onto the sample holder of a Novocontrol Concept-40 system with an Alpha-A impedance analyzer. The frequency range of the measurement is from 10^7 Hz to 10^{-2} Hz. A Quatro Cryosystem temperature controller was applied with a temperature accuracy of ±0.1 K. The measurements were conducted from 313 to 253 K at an interval of 10 K and from 253 to 213 K at an interval of 5 K. A thermal annealing of 20 min was applied before each measurement to assure the thermal equilibrium.

The complex dielectric permittivity of the films, $\varepsilon^*(\omega)$, is analyzed through the Havriliak-Negami (HN) function:

$$\varepsilon^*(\omega) = \varepsilon'(\omega) - i\varepsilon''(\omega) = \varepsilon_\infty + \sum_k \frac{\Delta\varepsilon_k}{\left[1+(i\omega\tau_{HN,k})^{\beta_k}\right]^{\gamma_k}} + \frac{\sigma_{dc}}{i\varepsilon_0\omega} \quad (2)$$

where $\varepsilon'(\omega)$ and $\varepsilon''(\omega)$ are the storage permittivity and loss permittivity, respectively. ε_0 and ε_∞

156 are the vacuum permittivity and the dielectric constant at infinite high frequency, respectively. ω
157 is the angular frequency, σ_{dc} is the dc-conductivity, and $\Delta\varepsilon_k$, $\tau_{HN,k}$, β_k, and γ_k are the dielectric
158 relaxation strength, HN relaxation time, and the shape parameters of the k^{th} relaxation process.
159 The characteristic time of the k^{th} relaxation process of the films can then be extracted from the HN
160 relaxation time:

161 $$\tau_k = \tau_{HN,k}\left[sin\frac{\beta_k\pi}{2+2\gamma_k}\right]^{-1/\beta_k}\left[sin\frac{\beta_k\gamma_k\pi}{2+2\gamma_k}\right]^{1/\beta_k} \quad (3)$$

162 Pure-gas permeability of H_2, CH_4, N_2, and CO_2 was measured using a constant volume-
163 variable pressure apparatus at 35 °C [6, 35]. Both sides of the sample were degassed for ~14 h to
164 ensure the removal of water vapor. After the leak test, the sample was exposed to a feed gas at
165 three pressures (p_2 = 4.4, 7.9, and 11.3 bar), which are typical to study gas transport properties [36-
166 38]. Gas permeability coefficient (P_A) can be calculated using the following equation:

167 $$P_A = \frac{V_d l}{p_2 ART}\left[\left(\frac{dp_1}{dt}\right)_{ss} - \left(\frac{dp_1}{dt}\right)_{leak}\right] \quad (4)$$

168 where l and A are the film thickness and effective area, respectively. R is the gas constant, T is the
169 testing temperature (35 °C), and V_d is the downstream volume. The $(dp_1/dt)_{ss}$ and $(dp_1/dt)_{leak}$ are
170 the increasing rate of the downstream pressure at the feed pressure of p_2 and 0, respectively. The
171 permeation measurement follows the order of N_2, CH_4, H_2, and CO_2, and sometimes N_2 was re-
172 tested to ensure that the samples remain intact. The tests can last 5-7 days, while the sample was
173 kept under vacuum or with dry gas. Gas permeability has an uncertainty of less than 10% estimated
174 using an error propagation analysis [39].

175 Pure-gas solubility was measured using a microbalance (IGA 001, Hiden Isochema,
176 Warrington, UK) at 35 °C and three pressures (p_A = 4.5, 7.9, and 11.4 bar) [5]. About 80 mg of the
177 samples were used, and gas sorption (C_A, cm^3 (STP) cm^{-3}) was calculated from the mass change

178 of the samples after reaching an equilibrium considering the buoyancy effect (cf. Equations S1 and
179 S2). Gas solubility (S_A, cm^3 (STP) cm^{-3} atm^{-1}) can be calculated using the following equation:

180 $$S_A = C_A/p_A \quad (5)$$

181 Gas transport through polymeric materials follows the solution-diffusion mechanism, and
182 thus, gas diffusivity (D_A, cm^2/s) can be expressed as:

183 $$D_A = P_A/S_A \quad (6)$$

184 The gas solubility and diffusivity have an uncertainty of <10% and <14%, respectively,
185 estimated using the propagation analysis of error [36, 39].

186

187 **3. Results and Discussion**

188 **3.1. Physical and chemical properties of supramolecular networks**

189 Fig. 1a presents the schematic of the XLPEO by photopolymerization of 20 mass%
190 PEGDA and 80 mass% PEGMEA. Fig. 1b shows the structure of $LiClO_4$, $Ni(BF_4)_2$, and $Cu(BF_4)_2$.
191 The salts appear to be dissolved in XLPEO, as evidenced by the transparent and uniform films (cf.
192 Fig. 1c).

193 Table 1 compares the anhydrous salt content in XLPEO/$Ni(BF_4)_2$ calculated from the
194 prepolymer solutions (x, mass%) and measured using XRF (x_{XRF}, mass%). Both values are similar,
195 suggesting that the water molecules in the hydrated salt were removed by dissolving in XLPEO
196 and drying. For convenience, the calculated x values are used for further modeling in this study.

197

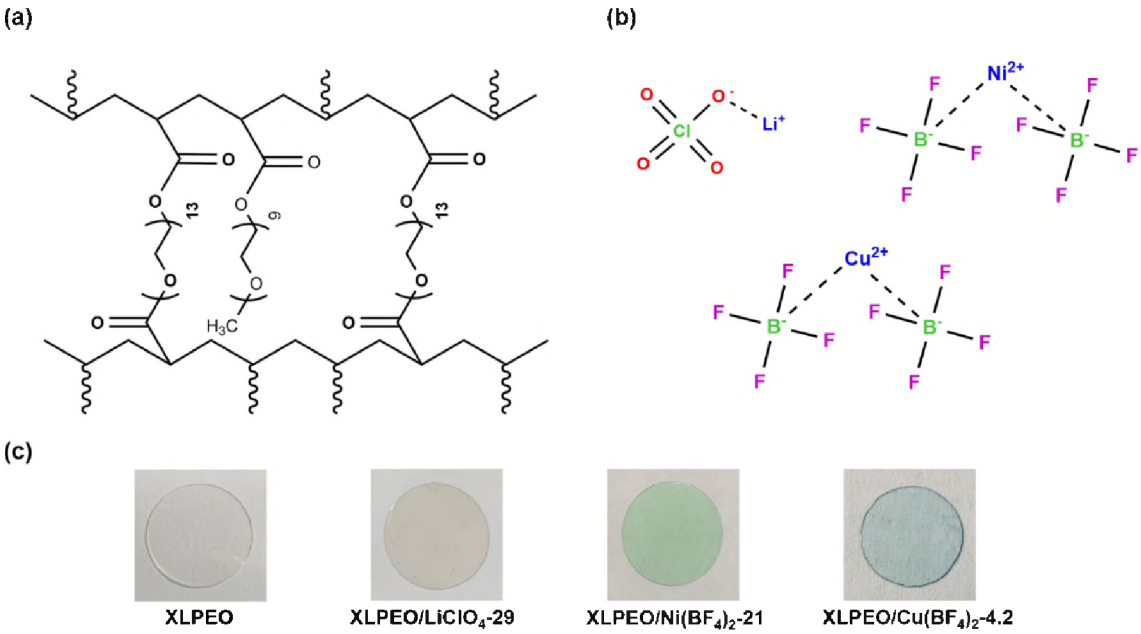

Figure 1. (a) Schematic of XLPEO prepared from PEGDA and PEGMEA. (b) Structure of $LiClO_4$, $Ni(BF_4)_2$, and $Cu(BF_4)_2$. (c) Photos of the XLPEO/salt films.

Table 1. Physical properties for XLPEO/$Ni(BF_4)_2$ (x, mass%) including r (molar ratio of the ether oxygens to the metal ions), ρ_{PE}, T_g, and pure-gas permeability and selectivity at 35 °C.

x (%)	x_{XRF} (%)	r	ρ_{PE} (g/cm^3)	T_g (°C)	P_A (Barrer)				CO_2/gas selectivity			
					N_2	H_2	CH_4	CO_2	N_2	H_2	CH_4	C_2H_6
0	0	0	1.149	-63	10	45	33	520	52	11	16	6.2
1.4	-	371	1.157	-60	7.7	36	25	400	53	11	16	-
6.4	7.2	77	1.208	-50	3.8	29	11	190	51	6.7	18	-
12	14	39	1.251	-33	2.4	20	6.7	90	38	4.4	14	9.3
17	18	26	1.301	-13	0.76	7.5	1.2	21	28	2.8	18	12
21	21	20	1.345	3.0	0.27	3.4	0.37	5.9	22	1.7	16	-

Fig. 2a exhibits the FTIR spectra of XLPEO/$Ni(BF_4)_2$. Pure $Ni(BF_4)_2$ crystals present a vibration peak at 1632 cm^{-1}, which disappears in the XLPEO/$Ni(BF_4)_2$, indicating the almost complete dissociation of $Ni(BF_4)_2$. Additionally, as the salt concentration increases, the peak at

209 1096 cm^{-1} representing the C−O bond vibration in XLPEO shifts to lower wavenumbers, which
210 can be ascribed to the weakened C-O bond caused by the interaction with the cations [27, 40]. For
211 example, the introduction of 12 mass% and 21 mass% of $Ni(BF_4)_2$ lowers C−O stretching
212 frequency to 1071 and 1057 cm^{-1}, respectively. On the other hand, increasing the $Ni(BF_4)_2$
213 concentration has a minimal effect on the C=O stretching frequency at 1732 cm^{-1}, indicating the
214 absence of strong interactions between the C=O and Ni^{2+}. Similar behavior has been observed for
215 XLPEO/$LiClO_4$ (Fig. S1a of Supporting Information). Additionally, adding <4.2 mass% $Cu(BF_4)_2$
216 to XLPEO has an insignificant effect on the C–O bond (Fig. S1b) because the loadings are too low
217 for FTIR to detect. As an example, Fig. S1c also displays the spectra of XLPEO/$Ni(BF_4)_2$ at high
218 wavenumbers. The appearance of the peaks at ~3500 cm^{-1} indicates the water sorption due to the
219 sorption of the water vapor from the atmosphere.
220

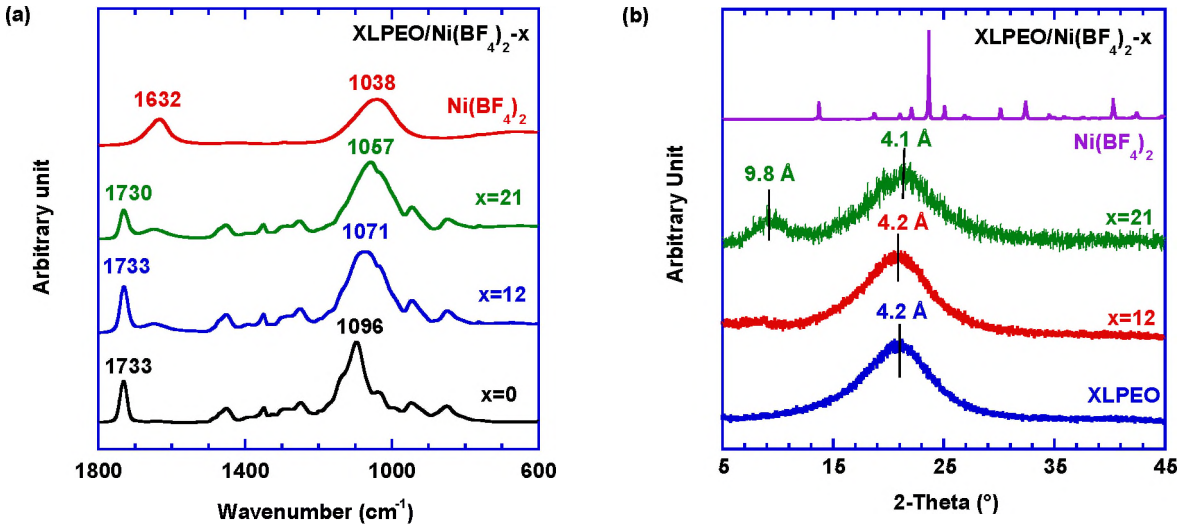

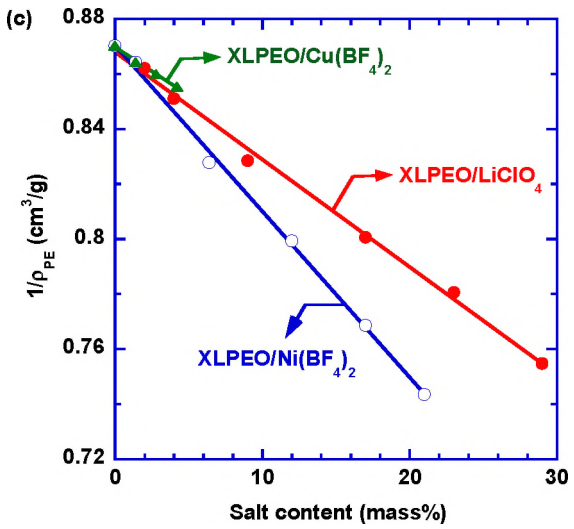

Figure 2. Comparison of (a) FTIR spectra and (b) XRD patterns for XLPEO, $Ni(BF_4)_2$, XLPEO/$Ni(BF_4)_2$-17, and XLPEO/$Ni(BF_4)_2$-29. (c) Correlation between the ρ_{PE} and salt content. The lines are the best fit using Equation 7.

Fig. 2b displays the WAXD spectra of XLPEO/$Ni(BF_4)_2$. Pure $Ni(BF_4)_2$ exhibits sharp peaks because of its crystalline structure, which disappear in the polymer electrolytes, indicating that the salt is solvated by XLPEO and becomes amorphous. XLPEO is amorphous at ≈ 23 °C and shows a broad peak at 2θ of 21° (corresponding to a *d*-space of 4.2 Å). The addition of $Ni(BF_4)_2$ has a negligible effect on the *d*-spacing, and similar behavior has been observed for XLPEO/$LiClO_4$ (Figure S1c). On the other hand, higher $Ni(BF_4)_2$ loading seems to generate a new peak at 2θ of 9° (corresponding to a *d*-spacing of 9.8 Å), which might be due to complexes of XLPEO with Ni^{2+} [41].

Fig. 2c presents the effect of the salt content on the density of the samples (ρ_{PE}). The density values are also recorded in Tables 1 and S1. Increasing the salt content increases the density, which can be described using an additive model [27]:

$$\frac{1}{\rho_{PE}} = \frac{w_P}{\rho_P} + \frac{w_S}{\rho_S} = \frac{1}{\rho_P} + \left(\frac{1}{\rho_S} - \frac{1}{\rho_P}\right) w_S \quad (7)$$

where ρ_P and ρ_S are the density of XLPEO and the dissociated amorphous salt, respectively. The

239 w_P and w_S are the mass fraction of the XLPEO and salt in the supramolecular networks,
240 respectively. As shown in Fig. 2c, the fitting yields a ρ_S value of 2.10 g/cm^3 for amorphous $LiClO_4$,
241 2.31 g/cm^3 for amorphous $Ni(BF_4)_2$, and 1.93 g/cm^3 for amorphous $Cu(BF_4)_2$. The ρ_S for
242 amorphous $LiClO_4$ is within 5% of the value of 2.20 g/cm^3 previously reported [27] for amorphous
243 $LiClO_4$ and is lower than the crystal density of 2.42 g/cm^3 (provided by Aldrich) because the
244 crystalline phase has a more compact structure than the amorphous phase. To the best of our
245 knowledge, there are no reported density values for anhydrous crystalline or dissociated
246 amorphous $Ni(BF_4)_2$ or $Cu(BF_4)_2$.

247 PALS results provide two parameters to characterize the free volume, i.e., o- Ps lifetime
248 (τ_3) indicating the size of the free volume element, and intensity (I_3) representing the relative
249 number of the free volume elements [5, 7]. The lifetimes are correlated with the radii (r, Å) of the
250 free volume elements using the Tao-Eldrup equation:

251 $$\tau_3 = \frac{1}{2}\left[1 - \frac{r}{r+1.656} + \frac{1}{2\pi}\sin\left(\frac{2\pi r}{r+1.656}\right)\right]^{-1} \quad (8)$$

252 The average volume of a free volume element (V_f) can be calculated as follows:

253 $$V_f = \frac{4}{3}\pi r^3 \quad (9)$$

254 As shown in Table 2, increasing the salt content decreases the I_3, indicating fewer free
255 volume elements. The size of the free volume elements V_f and the relative fractional free volume
256 ($V_f \times I_3$) decrease with increasing $LiClO_4$ content, most noticeably for higher salt loading. For
257 example, the introduction of 9 mass% $LiClO_4$ to XLPEO decreases the average free volume from
258 147 to 130 Å^3. Similar results have been reported in polyether-based polymers on the addition of
259 $LiClO_4$ [42, 43] (Fig. S2), where loadings at or below 5 mass% do not alter or sometimes increase
260 the average free volume element size. Similarly, low loadings of $Cu(BF_4)_2$ increase the size of the
261 free volume elements for the loading range studied (≤4.2 mass%).

Table 2. PALS results for XLPEO/$LiClO_4$ and XLPEO/$Cu(BF_4)_2$-x.

XLPEO/salt-x	I_3 (%)	Free volume element size			$V_f \times I_3$
		τ_3 (ns)	r (Å)	V_f (Å^3)	
None	21.3±0.1	2.497±0.010	3.271±0.008	147	3122
$LiClO_4$-2	18.2±0.1	2.476±0.009	3.254±0.007	144	2621
$LiClO_4$-9	17.2±0.1	2.340±0.012	3.146±0.010	130	2240
$Cu(BF_4)_2$-1.4	21.7±0.1	2.497±0.018	3.271±0.014	147	3181
$Cu(BF_4)_2$-2.8	21.4±0.1	2.614±0.004	3.360±0.003	159	3401
$Cu(BF_4)_2$-4.2	21.2±0.2	2.608±0.005	3.355±0.004	158	3355

Fig. 3a,b presents the DSC thermograms of XLPEO/$LiClO_4$ and XLPEO/$Ni(BF_4)_2$, respectively. XLPEO shows a crystallization peak at -36 °C and a melting peak at -7 °C, consistent with the literature [7]. Interestingly, the doping of the salts eliminates the crystallization and melting of the XLPEO. Increasing the salt loading increases the T_g of the polymers because the dissociated cations form strong ion-dipole interactions with ether oxygens and act as cross-linkers [27]. The T_g values are recorded in Table 1 for XLPEO/$Ni(BF_4)_2$ and Table S1 for XLPEO/$LiClO_4$ and XLPEO/$Cu(BF_4)_2$.

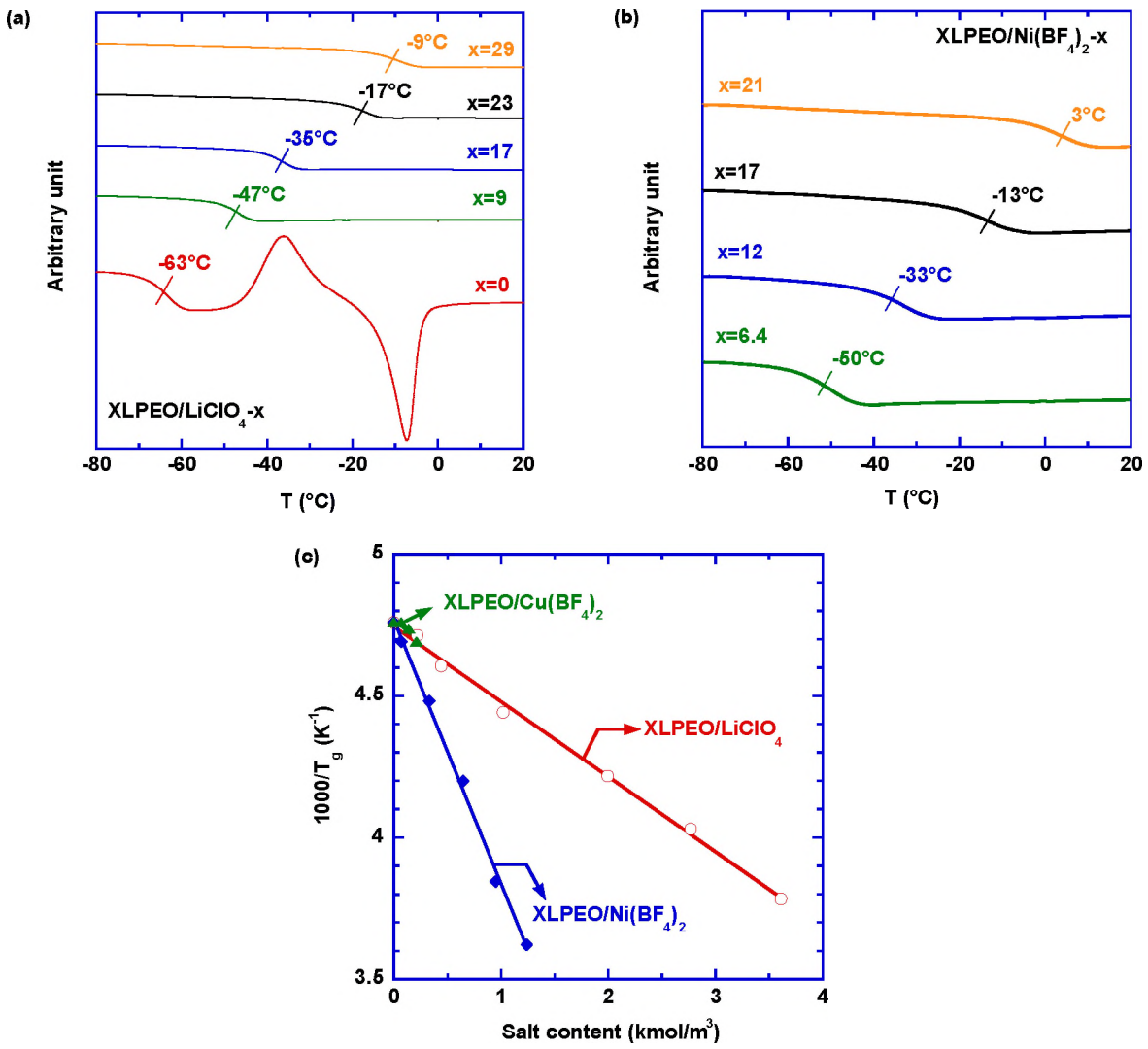

Figure 3. DSC curves of (a) XLPEO/$LiClO_4$ and (b) XLPEO/$Ni(BF_4)_2$. (c) Correlation between the T_g and salt content. The lines are the best fit using Equation 10.

The T_g of the metal ion-coordinated polymers can be described using an empirical equation [44, 45]:

$$1/T_g = 1/T_{g,P} - ac \tag{10}$$

where $T_{g,P}$ is the glass transition temperature for XLPEO (K), a is an adjustable constant, and c is the concentration of the salt (kmol m^{-3}). Fig. 3c shows that the effect of the salt loading on the T_g can be satisfactorily described using this model with a value of 2.6×10^{-4} m^3 $kmol^{-1}$ K^{-1} for

283 XLPEO/$LiClO_4$ and 9.3×10^{-4} m^3 $kmol^{-1}$ K^{-1} for XLPEO/$Ni(BF_4)_2$. The *a* value for XLPEO/$LiClO_4$
284 is very close to previously reported literature values (cf. Table S2 [27, 44]). The *a* value for
285 XLPEO/$LiClO_4$ is lower than that for XLPEO/$Ni(BF_4)_2$, indicating that the divalent Ni^{2+} ions are
286 more effective than monovalent Li^+ ions to cross-link XLPEO. For the limited composition range
287 studied here, divalent Cu^{2+} ions affect T_g similar to (or slightly less than) Li^+ ions in this XLPEO.
288 This result also indicates that the cross-linking by the cations is more influential on the polymer
289 chain flexibility than the plasticization effect by the anions (which tends to decrease the T_g).
290
291 **3.2. Gas transport properties of supramolecular networks**
292 Fig. 4a presents the effect of the feed pressure on pure-gas permeability in an example
293 XLPEO/$LiClO_4$-17 at 35 °C. Increasing the pressure increases CO_2 permeability because of the
294 plasticization and has a negligible effect on the permeability of H_2, N_2, and CH_4 because of their
295 low sorption, which are typical behaviors for rubbery polymers [7, 36].
296 Fig. 4b presents the effect of the $LiClO_4$ content in XLPEO on pure-gas permeability at
297 35 °C. XLPEO exhibits gas permeability values similar to the literature [7], while XLPEO/$LiClO_4$
298 shows very peculiar permeation properties at low loadings, i.e., gas permeability increases before
299 decreasing with increasing the $LiClO_4$ loading. For example, XLPEO/$LiClO_4$-2 shows a CO_2
300 permeability of 710 Barrer, which is 38% higher than the pure polymer (520 Barrer); by contrast,
301 further increase of the $LiClO_4$ loading to 4 mass% decreases CO_2 permeability to 230 Barrer
302 because of the increased $T_{g,PE}$. XLPEO/$Cu(BF_4)_2$ exhibits similar behavior of gas permeation (Fig.
303 4c). Introduction of 1.4 mass% $Cu(BF_4)_2$ increases the CO_2 permeability 70% from 520 to 880
304 Barrer, and further increase of salt loading to 2.8 mass% decreases the permeability to 380 Barrer.
305 By contrast, the addition of the $Ni(BF_4)_2$ consistently decreases gas permeability (cf. Table 1 and

Fig. S3a), which agrees well with its greater tendency in increasing T_g than the other two salts. For instance, XLPEO/$Ni(BF_4)_2$-1.4 and XLPEO/$Ni(BF_4)_2$-6.4 show CO_2 permeability of 400 and 190 Barrer, respectively. However, the reason for the unexpected enhancement of the gas permeability at low loadings is not clear, though Li^+ ions were reported to increase the photopolymerization rate and conversion of 1-vinylimidazole [46]. As the permeation measurement was conducted under vacuum or with dry gas for 5-7 days, we do not expect that there is any water vapor in the samples, which is also validated by the consistent behavior for all gases. Furthermore, if water vapor plays an important role, the samples with higher salt content are expected to be more hygroscopic and more susceptible to sorbed water. However, adding 21 mass% $Ni(BF_4)_2$ decreases CO_2 permeability from 520 to 5.9 Barrer, which suggests the absence of the water in the samples. More importantly, similar behavior has also been reported for MMMs containing MOFs [12] and MOPs [38], though no clear explanation was provided. Polymer dynamics are also studied and presented in Section 3.4 (Dynamics of supramolecular structures) to further elucidate the effect of salt loading.

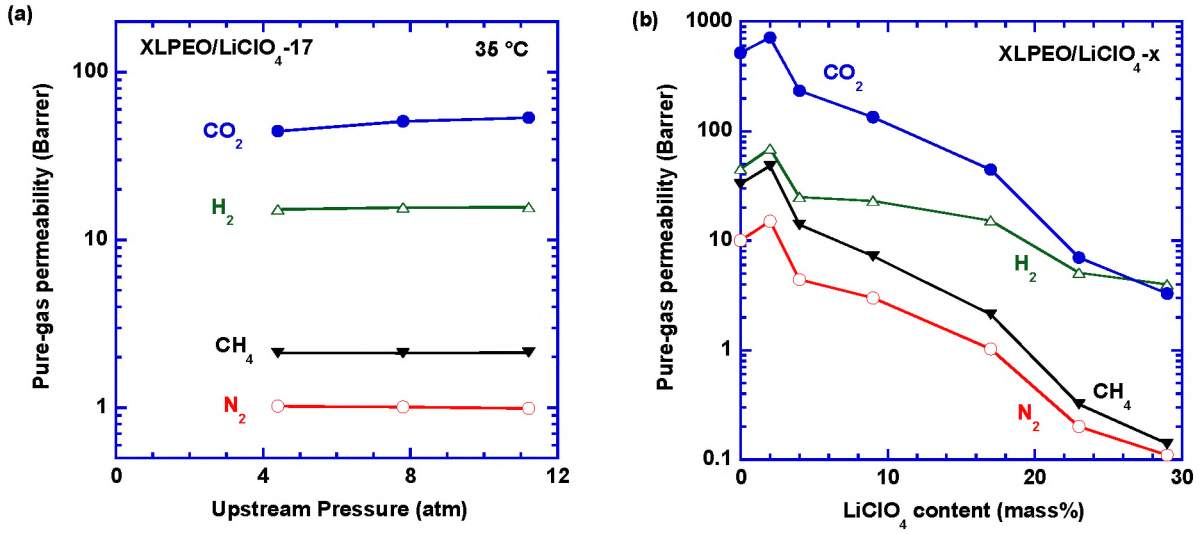

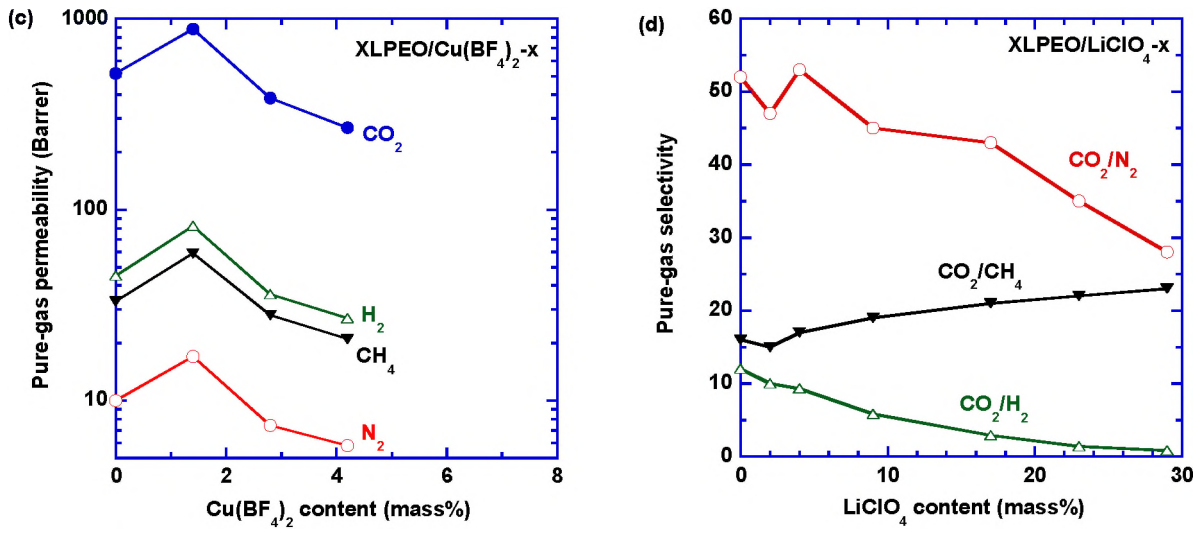

Figure 4. Pure-gas transport properties in XLPEO/salt at 35 °C. (a) Effect of the feed gas pressure on gas permeability in XLPEO/$LiClO_4$-17. Gas permeability as a function of the salt loading for (b) XLPEO/$LiClO_4$ and (c) XLPEO/$Cu(BF_4)_2$. (d) Effect of the $LiClO_4$ loading on CO_2/gas selectivity in XLPEO at 50 psig.

Fig. 4d shows that increasing the $LiClO_4$ content decreases CO_2/N_2 and CO_2/H_2 selectivity and increases CO_2/CH_4 selectivity. Similarly, increasing $Ni(BF_4)_2$ loading decreases CO_2/N_2 and CO_2/H_2 selectivity. However, the CO_2/CH_4 selectivity of XLPEO/$Ni(BF_4)_2$ is independent of the $Ni(BF_4)_2$ content (Fig. S3b). Fig. S3c shows that the $Cu(BF_4)_2$ content does not affect the CO_2/gas selectivity, probably because of the small composition change.

To further understand the effect of the salt content on gas transport properties, CO_2 and C_2H_6 sorption isotherms were determined at 35 °C and displayed in Fig. 5a,b for XLPEO/$LiClO_4$ and Fig. S4a,b,c for XLPEO/$Ni(BF_4)_2$. The sorption of H_2, N_2 and CH_4 in the samples is too low to detect using our apparatus. Therefore, C_2H_6 is used as a surrogate because it is more condensable and has higher sorption than H_2, N_2, and CH_4. More importantly, similar to H_2, N_2, and CH_4, C_2H_6 has no special interaction with the salts and polymer in this study. CO_2 and C_2H_6 sorption isotherms are linear, following Henry's law due to the rubbery nature of the samples [36].

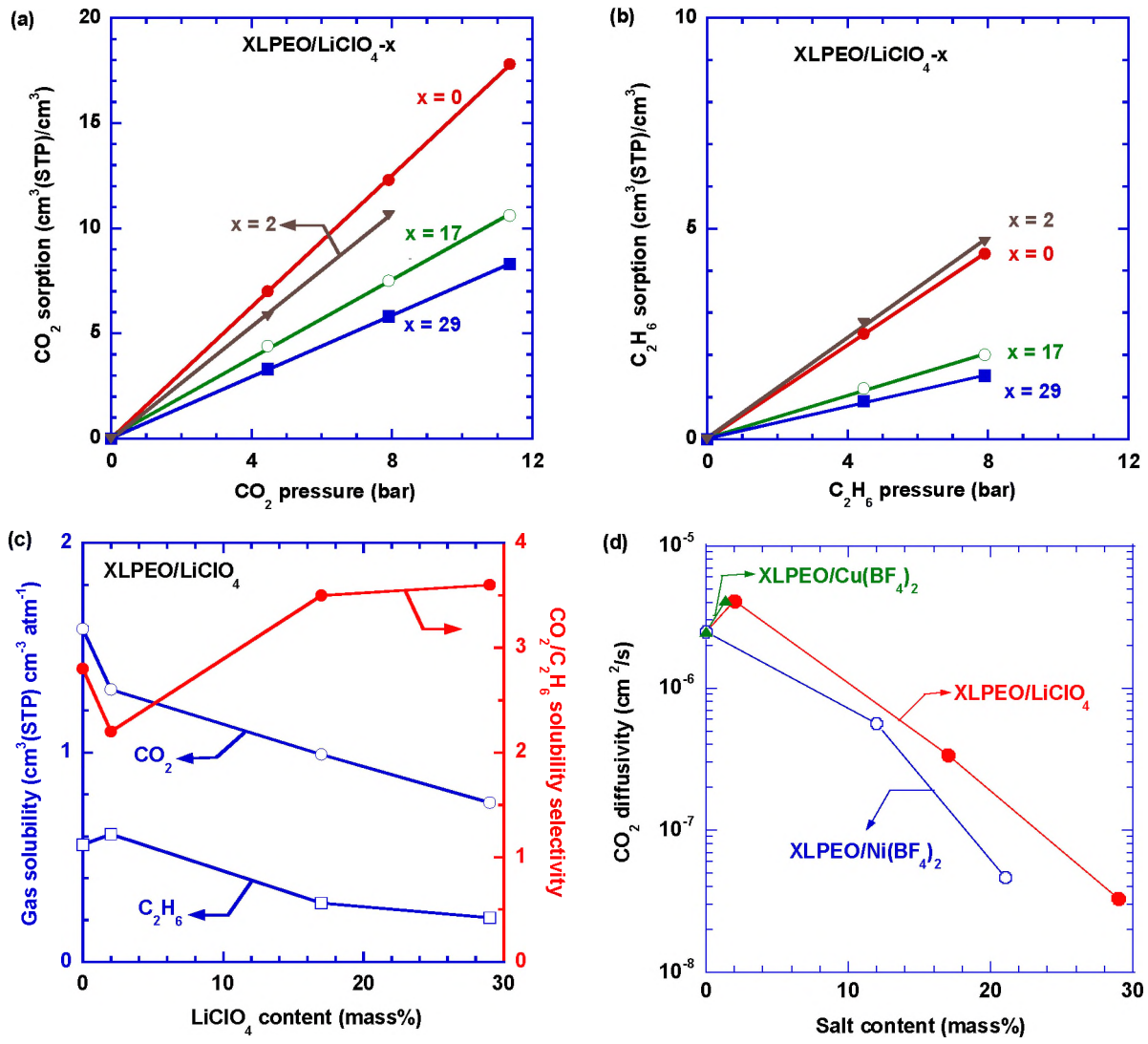

Figure 5. Pure-gas sorption and diffusion in XLPEO/salt at 35 °C. Effect of the $LiClO_4$ loading on (a) CO_2 sorption isotherms, (b) C_2H_6 sorption isotherms, and (c) CO_2 and C_2H_6 solubility and CO_2/C_2H_6 solubility selectivity of XLPEO/$LiClO_4$. (d) CO_2 diffusivity in XLPEO/$LiClO_4$ and XLPEO/$Ni(BF_4)_2$ as a function of the salt content.

CO_2 and C_2H_6 solubility at 35 °C was calculated using Equation 5, and the results are shown in Fig. 5c and recorded in Table S3. Low salt loadings (1.4 to 2 mass%) for XLPEO/$Cu(BF_4)_2$ and XLPEO/$LiClO_4$ cause no change (within error) in C_2H_6 solubility and for XLPEO/$Cu(BF_4)_2$ no change in CO_2 solubility. This result is in contrast to all loadings of $Ni(BF_4)_2$ and higher loadings of $LiClO_4$, which significantly decrease CO_2 and C_2H_6 solubility monotonically and similarly for both salts. For example, as $LiClO_4$ loading increases to 29 mass%

in XLPEO, CO_2 solubility decreases from 1.6 to 0.76 cm^3(STP) cm^{-3} atm^{-1}, and C_2H_6 solubility decreases from 0.56 to 0.21 cm^3(STP) cm^{-3} atm^{-1}. The introduced metal ions coordinate with ether oxygens in XLPEO, lowering the free volume (as indicated by the increased T_g) and lessening the affinity of the ether oxygens towards CO_2. The T_g results in Fig. 3c might suggest that Ni^{2+} coordination would be more effective in lowering solubility (than Li^+), but this trend is not observed. The decreased CO_2 and C_2H_6 solubility with increasing salt content is attributed to decreased free volume in the networks (cf. Fig. S4d). Moreover, increasing the salt content increases the CO_2/C_2H_6 solubility selectivity for both XLPEO/$LiClO_4$ and XLPEO/$Ni(BF_4)_2$, presumably because C_2H_6 has a larger critical volume (148.3 cm^3/mol) than CO_2 (93.9 cm^3/mol), and its sorption can be more severely restricted by the decreased free volume.

The CO_2 and C_2H_6 diffusion coefficient is calculated using Equation 6, and the results are shown in Fig. 5d and Table S3. Low salt loadings (1.4 to 2 mass%) for XLPEO/$Cu(BF_4)_2$ and XLPEO/$LiClO_4$ increase diffusivity. All salt loadings examined in XLPEO/$Ni(BF_4)_2$ and higher salt loadings in XLPEO/$LiClO_4$ decrease diffusivity. The diffusivity decrease is attributed to the decreased chain flexibility (as indicated by the increased T_g) and free volume of the supramolecular networks (as indicated by the PALS results in XLPEO/$LiClO_4$).

3.3. Modeling of gas transport properties of supramolecular networks

Gas diffusion in polymeric materials can be described using the free volume model [47-49]:

$$D_A = D_{A,0} exp\left(-\frac{B_A}{FFV}\right) \quad (11)$$

where $D_{A,0}$ is a front factor, B_A depends on the penetrant size, and FFV is the fractional free volume of the polymers. The FFV is defined as follows:

$$FFV = \frac{V-V_0}{V} = 1 - \rho V_0 \quad (12)$$

where V is the specific volume at T, and V_0 is the occupied volume at 0 K estimated as 1.3 times of the van der Waals volume. For rubbery polymers, FFV can be estimated using Equation 13 [4, 48, 50]:

$$FFV = FFV(T_g) + \alpha_r(T - T_g) \quad (13)$$

where $FFV(T_g)$ is the apparent FFV at T_g, and α_r is the expansion coefficient of the polymer. For the XLPEO samples, the $FFV(T_g)$ was estimated to be 0.055, and α_r is 8.4×10^{-4} K^{-1} [4, 48, 50].

Combining Equations 11 and 13 yields the T_g-integrated free volume model:

$$D_A = D_{A,0} exp\left(\frac{-B_A/\alpha_r}{FFV(T_g)/\alpha_r + (T-T_g)}\right) \quad (14)$$

This equation has the same form as the Vogel -Tammann-Fulcher (VTF) equation, which has been used to describe the transport of ions in rubbery polymers. Thus, B_A/α_r is related to the activation energy for diffusion (i.e., $E_{D,A}/R = B_A/\alpha_r$), and $FFV(T_g)/\alpha_r$ is the deviation (≈50 K) of the determined T_g from the ideal T_g [51]. This model is also expected to describe the effect of anions on the gas diffusivity, particularly when their effect on the T_g is incorporated in Equation 10.

Equation 14 has been used to describe CO_2 diffusivity in XLPEO prepared from PEGDA and PEGMEA at various compositions and temperatures [4, 48], as shown in Fig. 6a. The curve is the best fit based on the PEGDA-*co*-PEGMEA with the $D_{A,0}$ value of 5.5×10^{-3} cm^2/s, $E_{D,A}$ value of 11 kJ/mol (Table S4), and $FFV(T_g)/\alpha_r$ value of 50 K. Interestingly, the CO_2 diffusivity in XLPEO/$LiClO_4$ can be well described by the model, which is remarkable considering no adjustable parameters are used. On the other hand, the model underestimates the CO_2 diffusivity in XLPEO/$Ni(BF_4)_2$, which might be related to the additional *d*-spacing (9.8 Å) from the

complexes. The XLPEO/$Ni(BF_4)_2$ behaves as a stronger (or less fragile, less coupled) system than XLPEO/$LiClO_4$ [52].

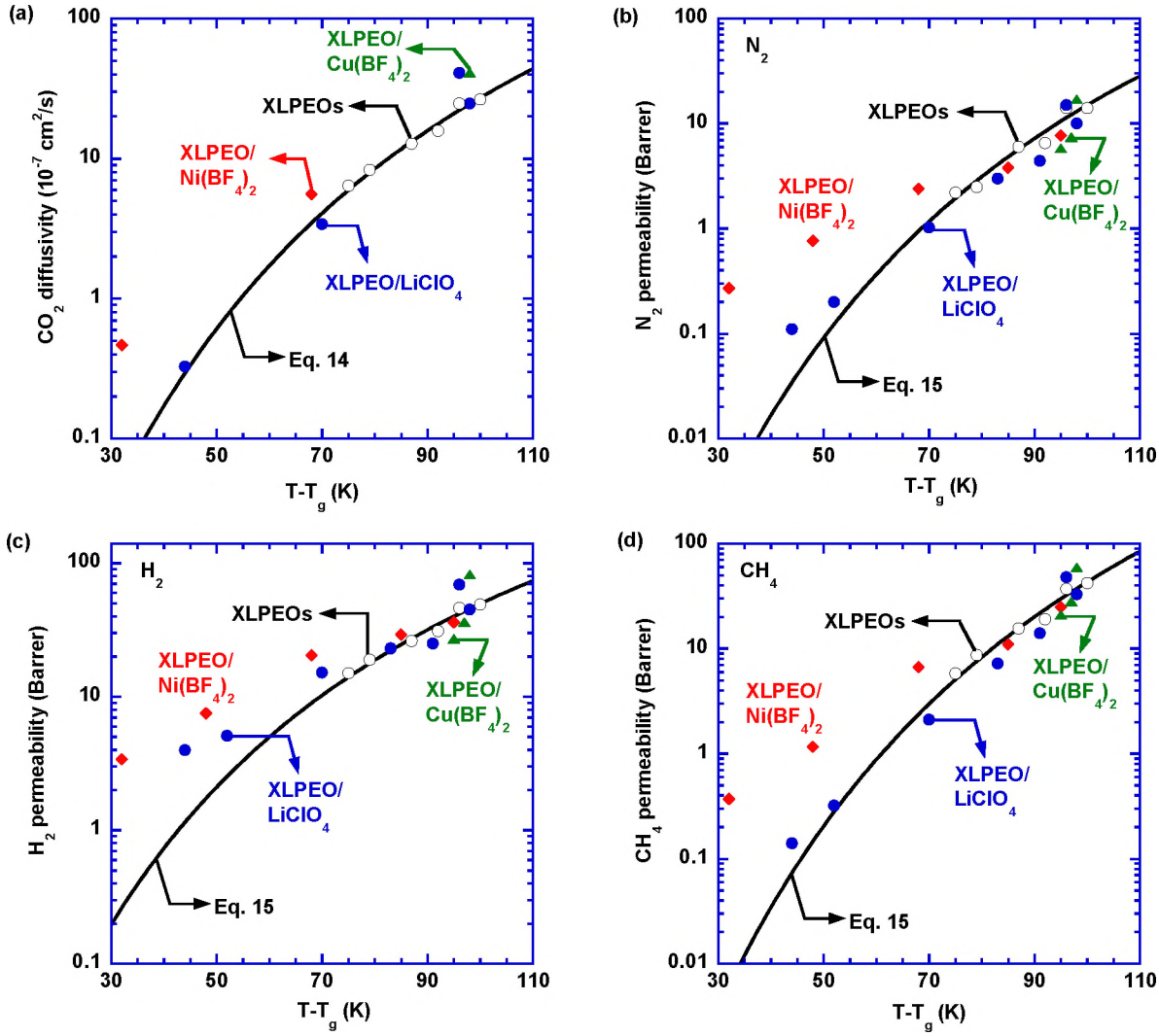

Figure 6. (a) CO_2 diffusivity as a function of (T - T_g) using Equation 14, where T is 308 K. Pure-gas permeability of (b) N_2, (c) H_2, and (d) CH_4 as a function of (T - T_g) at 35 °C based on Equation 15.

For light gases such as N_2, H_2, and CH_4, gas solubility in polymers is assumed to be independent of the free volumes, and therefore, Equation 14 can be written as:

$$P_A = P_{A,0} exp\left[\frac{-B_A/\alpha_r}{FFV(T_g)/\alpha_r + (T - T_g)}\right] \quad (15)$$

where $P_{A,0}$ is an adjustable constant independent of the composition of XLPEO/salt. This approach has been adopted previously to correlate light gas permeability and T_g in PEGDA-*co*-PEGMEA [48], as shown by the curves in Fig. 6b,c,d. Similar to CO_2 diffusivity, the permeability of light gases can be satisfactorily modeled for XLPEO/$LiClO_4$ and XLPEO/$Cu(BF_4)_2$, but it is underestimated for XLPEO/$Ni(BF_4)_2$. The parameters of $P_{A,0}$ and $E_{D,A}$ are also recorded in Table S4.

3.4. Dynamics of supramolecular structures

To elucidate the surprising effect of the low loadings of $LiClO_4$ and $Cu(BF_4)_2$ on improving gas diffusivity, dielectric measurements were conducted for XLPEO/$LiClO_4$ and XLPEO/$Cu(BF_4)_2$. Fig. 7a,b presents the derivative spectra of the XLPEO/$LiClO_4$ with salt concentrations from 0.1 mass% to 4 mass% and the XLPEO/$Cu(BF_4)_2$ with salt concentrations of 1.4, 2.8, and 4.2 mass%. For polymer electrolytes with high ionic conductivity, the segmental relaxation process is often shielded and not easy to detect [53]. To suppress the influence of the dc-conductivity, derivative spectra analysis is adopted with $\varepsilon'_{der}(\omega) = -\frac{\pi}{2}\frac{\partial ln\varepsilon'(\omega)}{\partial ln\omega}$ [54].

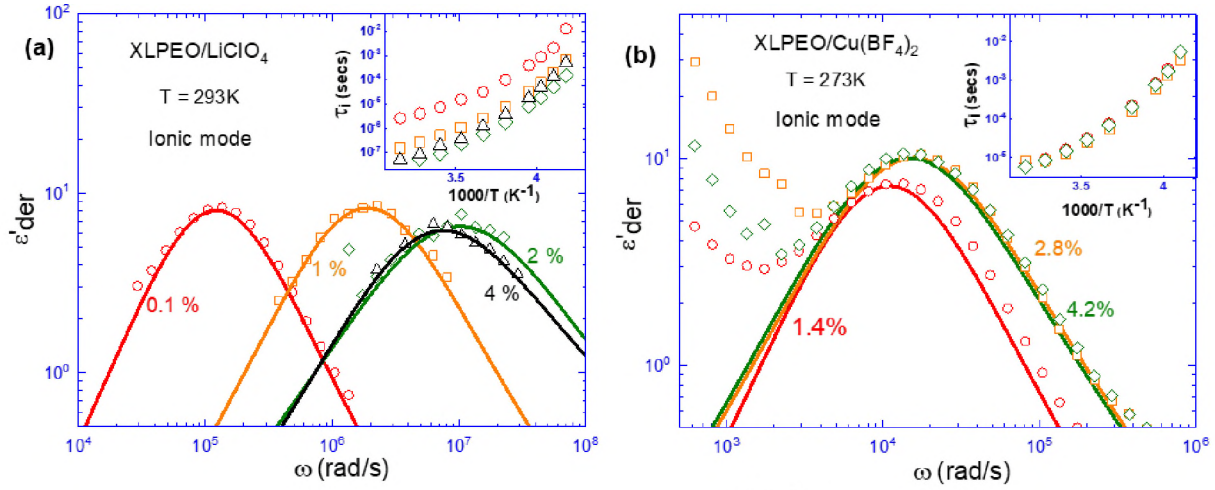

Figure 7. The dielectric derivative spectra, $\varepsilon'_{der}(\omega) = -\frac{\pi}{2}\frac{\partial ln\varepsilon'(\omega)}{\partial ln\tau\omega}$, of (a) XLPEO/$LiClO_4$ and (b)

XLPEO/$Cu(BF_4)_2$. The characteristic peak frequencies of the ionic modes of XLPEO/$LiClO_4$ depend strongly on the salt concentration. A non-monotonic shift of the peak position was observed, where the fastest ionic mode takes place at a salt concentration of ≈ 2 mass%. For XLPEO/$Cu(BF_4)_2$, the ionic peak exhibits smaller dependence on the salt concentration.

In XLPEO/$LiClO_4$, only ionic modes were observed that have a characteristic time, τ_i. The structural relaxations of XLPEO/$LiClO_4$ are not detectable due to the high ionic conductivity and the high cross-linking density of the XLPEO matrix. For PEO/Li^+ polymer electrolytes, however, the ionic conductivity is known to couple with the segmental relaxation of the polymer [55]. Therefore, one can obtain the relative relationship of the structural relaxation time of XLPEO/$LiClO_4$ of different salt loadings from the relaxation times of the ion motions. Interestingly, the ionic conductivities of XLPEO/$LiClO_4$ exhibit a non-monotonic change with the salt concentration with temperature. Below 2 mass%, the ionic relaxation time decreases dramatically with the increment of the loading. For instance, the ionic relaxation time of XLPEO/$LiClO_4$ at room temperature is around 8×10^{-6} s at 0.1 mass% salt loading that speeds up about 100 times to 8×10^{-8} s at 2 mass% salt loading. An increase in the salt concentration from 2 to 4 mass% does not lead to a further enhancement in dynamics but offers two times slowing down in the ionic relaxation. Note that the dramatic speeding up in dynamics at T = 293 K is not anticipated given the steady increase in T_g of XLPEO/$LiClO_4$ with salt content.

To understand the speed up in structural dynamics for XLPEO/$LiClO_4$ electrolytes, we analyze the temperature dependence of τ_i for the four XLPEO/$LiClO_4$ compositions. As shown in the inset of Fig. 7a, the fastest relaxation is measured for XLPEO/$LiClO_4$ with 2 mass% salt concentrations over the temperature range from 315 K down to temperatures approaching T_g. Only at the highest temperature close to 23 °C, do the 2 mass% and 4 mass% materials exhibit similarly fast dynamics, pointing to a salt-solvation induced plasticization effect on the polymer dynamics.

448 The increase in salt solvation upon heating up has been well-documented in polymer electrolytes,
449 as evidenced by a higher free-ion concentration at a higher temperature [56]. Fast dynamic
450 behavior has been observed in XLPEO/$Cu(BF_4)_2$, although only a mild speeding up (~1.2-1.5
451 times) in dynamics was observed for XLPEO/$Cu(BF_4)_2$ from 1.4 mass% to 2.8 mass% salt loading.
452 Again, as shown in the inset of Fig. 7b, the fastest relaxation is measured for XLPEO/$Cu(BF_4)_2$
453 with 2.8 mass% salt concentration over the temperature range from 273 K down to temperatures
454 approaching T_g, and only at the higher temperatures do the materials exhibit similarly fast
455 dynamics. The mildness of the speeding up in dynamics in XLPEO/$Cu(BF_4)_2$ may be due to the
456 nature of the interaction between Cu^{2+} and the XLPEO matrix.

457 The non-monotonic changes in ionic relaxation rates at low salt loadings are most likely
458 linked to the non-monotonic changes of the gas transport properties (the single-gas permeability)
459 of XLPEO/$LiClO_4$ and XLPEO/$Cu(BF_4)_2$. Polymer dynamics as well as gas and ion transport
460 properties in polymers are linked to the accessible static and dynamic free volume [57, 58].
461 Variables known to affect polymer dynamics and free volume include polymer architecture,
462 crystallinity, plasticization, antiplasticization, moisture and solvent absorption, additives,
463 crosslinking, strain, molecular weight, temperature, and pressure [58]. In this study, the metal ion-
464 polymer interaction is the critical variable that allows assessment of the effects of this interaction
465 on free volume, dynamics, and gas transport. The three salts are shown to complex the polymer
466 ether oxygens based on FTIR and T_g results, and for the most part, the effects of salt dissolution
467 and complexation are additive with salt content. The glass transition results (Fig. 3c) indicate that
468 Ni^{2+} is a more effective cross-linker than Li^+, which behaves similar to Cu^{2+} at the concentrations
469 studied here. The PALS results indicate that low levels of $LiClO_4$ (2 mass%) and $Cu(BF_4)_2$ (1.4
470 mass%) have little effect on the free volume element size, and in the case of $Cu(BF_4)_2$ (2.8 and 4.2

471 mass%) increase the free volume element size.

472

473 **4. Conclusion**

474 We demonstrate that XLPEO can be coordinated by metal cations such as Li^+, Ni^{2+}, and
475 Cu^{2+} to form amorphous supramolecular networks. The cation coordination increases T_g and
476 decreases gas diffusivity and permeability at high salt loadings. Surprisingly, the low loading of
477 $LiClO_4$ and $Cu(BF_4)_2$ (2 mass% or less) can increase the gas permeability as high as 70% and has
478 no impact on the CO_2/gas selectivity. By contrast, increasing the $Ni(BF_4)_2$ content consistently
479 decreases the gas permeability. Increasing the salt content decreases both CO_2 and C_2H_6 solubility
480 but increases CO_2/C_2H_6 solubility selectivity. Gas diffusivity and permeability of XLPEO/$LiClO_4$
481 and XLPEO/$Cu(BF_4)_2$ are successfully modeled as a function of T_g of the supramolecular networks
482 using a T_g-integrated free volume model (with the same form as the VTF equation) without
483 adjustable parameters, while the model underpredicts gas diffusivity and permeability of
484 XLPEO/$Ni(BF_4)_2$ suggesting that Ni^{2+} complexation of XLPEO leads to a less fragile, more highly
485 decoupled system. The PALS free volume element sizes are additive or larger than predicted by
486 additivity for low salt loadings in XLPEO/$LiClO_4$ and XLPEO/$Cu(BF_4)_2$. The salt loading also has
487 a non-monotonic influence on the polymer dynamics in dielectric measurements, validating the
488 unexpected effect on the gas transport properties. These results can be useful in designing MMMs
489 for superior gas separation properties and may also benefit developments in solid polymer
490 electrolytes and corrosion protective coatings.

491

492 **Acknowledgments**

493 We acknowledge the financial support of the U.S. Department of Energy National

Energy Technology Laboratory (NETL # DE-FE0031736) and the U.S. National Science Foundation (NSF #1554236). S.C. acknowledges the support of the Michigan State University startup fund for this research.

References

[1] B. Zhu, X. Jiang, S. He, X. Yang, J. Long, Y. Zhang, L. Shao. Rational design of poly(ethylene oxide) based membranes for sustainable CO_2 capture. J. Mater. Chem. A. 8 (2020) 24233-24252.

[2] J. Liu, X. Hou, H. Park, H. Lin. High-performance polymers for membrane CO_2/N_2 separation. Chem. Eur. J. 22 (2016) 15980-15990.

[3] H. Lin, E. Van Wagner, B. D. Freeman, L. G. Toy, R. P. Gupta. Plasticization-enhanced hydrogen purification using polymeric membranes. Science. 311 (2006) 639-642.

[4] H. Lin, B. D. Freeman. Materials selection guidelines for membranes that remove CO_2 from gas mixtures. J. Mol. Struct. 739 (2005) 57-74.

[5] J. Liu, S. Zhang, D. Jiang, C. M. Doherty, A. J. Hill, C. Cheng, H. Park, H. Lin. Highly polar but amorphous polymers with robust membrane CO_2/N_2 separation performance. Joule. 3 (2019) 1881-1894.

[6] D. Tian, T. Alebrahim, G. K. Kline, L. Chen, H. Lin, C. Bae. Structure and gas transport characteristics of triethylene oxide - grafted polystyrene - b - poly(ethylene - co - butylene) - b - polystyrene. J. Polym. Sci. 58 (2020) 2654-2663.

[7] H. Lin, E. Van Wagner, J. S. Swinnea, B. D. Freeman, S. J. Pas, A. J. Hill, S. Kalakkunnath, D. S. Kalika. Transport and structural characteristics of crosslinked poly(ethylene oxide) rubbers. J. Membr. Sci. 276 (2006) 145-161.

[8] T. Lee, J. Oh, J. Jang, F. Moghadam, J. Roh, S. Yoo, Y. Kim, T. H. Choi, H. Lin, H. Kim, H. Park. Elucidating the role of embedded metal-organic frameworks in water and ion transport properties in polymer nanocomposite membranes. Chem. Mater. 32 (2020) 10165-10175.

[9] Q. Xin, W. Shao, Q. Ma, X. Ye, Z. Huang, B. Li, S. Wang, H. Li, Y. Zhang. Efficient CO_2 separation of multi-permselective mixed matrix membranes with a unique interfacial structure regulated by mesoporous nanosheets. ACS Appl. Mater. Interfaces. 12 (2020) 48067-48076.

[10] A. Sabetghadam, X. Liu, S. Gottmer, L. Chu, J. Gascon, F. Kapteijn. Thin mixed matrix and dual layer membranes containing metal-organic framework nanosheets and Polyactive^{TM} for CO_2 capture. J. Membr. Sci. 570 (2019) 226-235.

[11] K. Xie, Q. Fu, P. A. Webley, G. G. Qiao. MOF scaffold for a high-performance mixed-matrix membrane. Angew. Chem. Int. Ed. 57 (2018) 8597-8602.

[12] X. Jiang, S. W. Li, S. S. He, Y. P. Bai, L. Shao. Interface manipulation of CO_2-philic composite membranes containing designed UiO-66 derivatives towards highly efficient CO_2 capture. J. Mater. Chem. A. 6 (2018) 15064-15073.

[13] J. Shen, M. Zhang, G. Liu, K. Guan, W. Jin. Size effects of graphene oxide on mixed matrix membranes for CO_2 separation. AIChE J. 62 (2016) 2843-2852.

[14] Q. Qian, P. A. Asinger, M. J. Lee, G. Han, K. Mizrahi Rodriguez, S. Lin, F. M. Benedetti, A. X. Wu, W. Chi, Z. P. Smith. MOF-based membranes for gas separations. Chem. Rev. 120 (2020) 8161-8266.

[15] R. Lin, B. V. Hernandez, L. Ge, Z. Zhu. Metal organic framework based mixed matrix membranes: an overview on filler/polymer interfaces. J. Mater. Chem. A. 6 (2018) 293-312.

[16] B. Seoane, J. Coronas, I. Gascon, M. E. Benavides, O. Karvan, J. Caro, F. Kapteijn, J. Gascon. Metal-organic framework based mixed matrix membranes: a solution for highly efficient CO_2 capture? Chem. Soc. Rev. 44 (2015) 2421-2454.

[17] V. J. Pastore, T. R. Cook. Coordination-driven self-assembly in polymer-inorganic hybrid materials. Chem. Mater. 32 (2020) 3680-3700.

[18] L. Hu, J. Liu, L. Zhu, X. Hou, L. Huang, H. Lin, J. Cheng. Highly permeable mixed matrix materials comprising ZIF-8 nanoparticles in rubbery amorphous poly(ethylene oxide) for CO_2 capture. Sep. Purif. Technol. 205 (2018) 58-65.

[19] C. R. P. Fulong, J. Liu, V. J. Pastore, H. Lin, T. R. Cook. Mixed-matrix materials using metal–organic polyhedra with enhanced compatibility for membrane gas separation. Dalton Trans. 47 (2018) 7905-7915.

[20] H. Wang, S. He, X. Qin, C. Li, T. Li. Interfacial engineering in metal-organic framework-based mixed matrix membranes using covalently grafted polyimide brushes. J. Am. Chem. Soc. 140 (2018) 17203-17210.

[21] R. Semino, J. C. Moreton, N. A. Ramsahye, S. M. Cohen, G. Maurin. Understanding the origins of metal-organic framework/polymer compatibility. Chem. Sci. 9 (2018) 315-324.

[22] P. Duan, J. C. Moreton, S. R. Tavares, R. Semino, G. Maurin, S. M. Cohen, K. Schmidt-Rohr. Polymer infiltration into metal-organic frameworks in mixed-matrix membranes detected in situ by NMR. J. Am. Chem. Soc. 141 (2019) 7589-7595.

[23] L. Voorhaar, R. Hoogenboom. Supramolecular polymer networks: hydrogels and bulk materials. Chem. Soc. Rev. 45 (2016) 4013-4031.

[24] Z. Qiao, S. Zhao, M. Sheng, J. Wang, S. Wang, Z. Wang, C. Zhong, M. D. Guiver. Metal-induced ordered microporous polymers for fabricating large-area gas separation membranes. Nat. Mater. 18 (2019) 163-168.

[25] Z. Xue, D. He, X. Xie. Poly(ethylene oxide)-based electrolytes for lithium-ion batteries. J. Mater. Chem. A. 3 (2015) 19218-19253.

[26] N. S. Schauser, R. Seshadri, R. A. Segalman. Multivalent ion conduction in solid polymer systems. Mol. Syst. Des. Eng. 4 (2019) 263-279.

[27] N. Paranjape, P. C. Mandadapu, G. Wu, H. Lin. Highly-branched cross-linked poly(ethylene oxide) with enhanced ionic conductivity. Polymer. 111 (2017) 1-8.

[28] I. Pinnau, L. G. Toy. Solid polymer electrolyte composite membranes for olefin/paraffin separation. J. Membr. Sci. 184 (2001) 39-48.

[29] D. Song, Y. Kang, S. Kang. Highly permeable and stabilized olefin transport membranes based on a poly(ethylene oxide) matrix and $Al(NO_3)_3$. J. Membr. Sci. 474 (2015) 273-276.

[30] T. C. Merkel, R. Blanc, I. Ciobanu, B. Firat, A. Suwarlim, J. Zeid. Silver salt facilitated transport membranes for olefin/paraffin separations: Carrier instability and a novel regeneration method. J. Membr. Sci. 447 (2013) 177-189.

[31] J. Deng, J. Yu, Z. Dai, L. Deng. Cross-linked PEG membranes of interpenetrating networks with ionic liquids as additives for enhanced CO_2 separation. Ind. Eng. Chem. Res. 58 (2019) 5261-5268.

[32] P. Madhavan, R. Sougrat, A. R. Behzad, K.-V. Peinemann, S. P. Nunes. Ionic liquids as self-assembly guide for the formation of nanostructured block copolymer membranes. J. Membr. Sci. 492 (2015) 568-577.
[33] X. Hu, J. Tang, A. Blasig, Y. Shen, M. Radosz. CO_2 permeability, diffusivity and solubility in polyethylene glycol-grafted polyionic membranes and their CO_2 selectivity relative to methane and nitrogen. J. Membr. Sci. 281 (2006) 130-138.
[34] A. Ghadimi, R. Gharibi, H. Yeganeh, B. Sadatnia. Ionic liquid tethered PEG-based polyurethane-siloxane membranes for efficient CO_2/CH_4 separation. Mater. Sci. Eng. C. 102 (2019) 524-535.
[35] L. Zhu, M. T. Swihart, H. Lin. Tightening polybenzimidazole (PBI) nanostructure via chemical cross-linking for membrane H_2/CO_2 separation. J. Mater. Chem. A. 5 (2017) 19914-19923.
[36] H. Lin, B. D. Freeman. Gas solubility, diffusivity and permeability in poly(ethylene oxide). J. Membr. Sci. 239 (2004) 105-117.
[37] J. D. Moon, A. T. Bridge, C. D'Ambra, B. D. Freeman, D. R. Paul. Gas separation properties of polybenzimidazole/thermally-rearranged polymer blends. J. Membr. Sci. 582 (2019) 182-193.
[38] J. Liu, C. R. P. Fulong, L. Hu, L. Huang, G. Zhang, T. R. Cook, H. Lin. Interpenetrating networks of mixed matrix materials comprising metal-organic polyhedra for membrane CO_2 capture. J. Membr. Sci. 606 (2020) 118122.
[39] P. R. Bevington, D. K. Robinson. Data reduction and error analysis for the physical sciences. 2nd ed. New York: McGraw-Hill, Inc.; 1992.
[40] K. Kim, L. Kuhn, I. V. Alabugin, D. T. Hallinan Jr. Lithium salt dissociation in diblock copolymer electrolyte using Fourier Transform Infrared Spectroscopy. Front. Energy Res. 8 (2020) 240.
[41] H. Goldansaz, D. Auhl, B. Goderis, Q. Voleppe, C. A. Fustin, J. F. Gohy, C. Bailly, E. van Ruymbeke. Transient metallosupramolecular networks built from entangled melts of poly(ethylene oxide). Macromolecules. 48 (2015) 3746-3755.
[42] M. Forsyth, P. Meakin, D. MacFarlane, A. Hill. Free volume and conductivity of plasticized polyether-urethane solid polymer electrolytes. J. Phys. Condens. Matter. 7 (1995) 7601.
[43] C. A. Furtado, G. G. Silva, J. Machado, M. Pimenta, R. Silva. Study of correlations between microstructure and conductivity in a thermoplastic polyurethane electrolyte. J. Phys. Chem. B. 103 (1999) 7102-7110.
[44] C. J. Hawker, F. K. Chu, P. J. Pomery, D. J. T. Hill. Hyperbranched poly(ethylene glycol)s: A new class of ion-conducting materials. Macromolecules. 29 (1996) 3831-3838.
[45] J. F. Lenest, A. Gandini, H. Cheradame. Crosslinked polyethers as media for ionic-conduction. Br. Polym. J. 20 (1988) 253-268.
[46] J. W. Whitley, W. J. Home, S. P. O. Danielsen, M. S. Shannon, J. E. Marshall, S. H. Hayward, C. J. Gaddis, J. E. Bara. Enhanced photopolymerization rate & conversion of 1-vinylimidazole in the presence of lithium bistriflimide. Eur. Polym. J. 60 (2014) 92-97.
[47] J. Park, D. R. Paul. Correlation and prediction of gas permeability in glassy polymer membrane materials via a modified free volume based group contribution method. J. Membr. Sci. 125 (1997) 23-39.
[48] H. Lin, B. D. Freeman, S. Kalakkunnath, D. S. Kalika. Effect of copolymer composition, temperature, and carbon dioxide fugacity on pure-and mixed-gas permeability in poly(ethylene glycol)-based materials: Free volume interpretation. J. Membr. Sci. 291

(2007) 131-139.
[49] H. Lin, M. Yavari. Upper bound of polymeric membranes for mixed-gas CO_2/CH_4 separations. J. Membr. Sci. 475 (2015) 101-109.
[50] L. Huang, J. Liu, H. Lin. Thermally stable, homogeneous blends of cross-linked poly (ethylene oxide) and crown ethers with enhanced CO_2 permeability. J. Membr. Sci. 610 (2020) 118253.
[51] Y. Karatas, R. D. Banhatti, N. Kaskhedikar, M. Burjanadze, K. Funke, H.-D. Wiemhöfer. Synthesis and modeling of polysiloxane-based salt-in-polymer electrolytes with various additives. J. Phys. Chem. B. 113 (2009) 15473-15484.
[52] M. Forsyth, D. R. Macfarlane, A. J. Hill. Glass transition and free volume behaviour of poly (acrylonitrile)/$LiCF_3SO_3$ polymer-in-salt electrolytes compared to poly (ether urethane)/$LiClO_4$ solid polymer electrolytes. Electrochim. Acta. 45 (2000) 1243-1247.
[53] F. Fan, Y. Wang, A. P. Sokolov. Ionic transport, microphase separation, and polymer relaxation in poly (propylene glycol) and lithium perchlorate mixtures. Macromolecules. 46 (2013) 9380-9389.
[54] M. Wübbenhorst, J. Van Turnhout. Analysis of complex dielectric spectra. I. One-dimensional derivative techniques and three-dimensional modelling. J. Non-Cryst. Solids. 305 (2002) 40-49.
[55] Y. Wang, F. Fan, A. L. Agapov, X. Yu, K. Hong, J. Mays, A. P. Sokolov. Design of superionic polymers—New insights from Walden plot analysis. Solid State Ion. 262 (2014) 782-784.
[56] Y. Wang, C.-N. Sun, F. Fan, J. R. Sangoro, M. B. Berman, S. G. Greenbaum, T. A. Zawodzinski, A. P. Sokolov. Examination of methods to determine free-ion diffusivity and number density from analysis of electrode polarization. Phys. Rev. E. 87 (2013) 042308.
[57] S. J. Pas, M. D. Ingram, K. Funke, A. J. Hill. Free volume and conductivity in polymer electrolytes. Electrochim. Acta. 50 (2005) 3955-3962.
[58] A. Hill, A. Thornton, R. Hannink, J. Moon, B. Freeman. Role of free volume in molecular mobility and performance of glassy polymers for corrosion-protective coatings. Corros. Eng. Sci. Technol. 55 (2020) 145-158.